CrossMark

RESEARCH PAPER

Pristine and Al-doped hematite printed films as photoanodes of *p*-type dye-sensitized solar cells

Mirko Congiu · Maria L. De Marco · Matteo Bonomo · Oswaldo Nunes-Neto · Danilo Dini · Carlos F.O. Graeff

Abstract We hereby propose a non-expensive method for the deposition of pure and Al-doped hematite photoanodes in the configuration of thin films for the application of dye-sensitized solar cells (DSSC). The electrodes have been prepared from hematite nanoparticles that were obtained by thermal degradation of a chemical precursor. The particles have been used in the preparation of a paste, suitable for both screen printing and doctor blade deposition. The paste was then spread on fluorine-doped tin oxide (FTO) to obtain porous hematite electrodes. The electrodes have been sensitized using N3 and D5 dyes and were characterized through current/voltage curves under simulated sun light (1 sun, AM 1.5) with a Pt counter electrode. Al-doping of hematite showed interesting changes in the physical and electrochemical characteristics of sensitized photoanodes since we could notice the growth of $AlFe_2O_4$ (hercynite) as a secondary crystal phase into the oxides obtained by firing the mixtures of two chemical precursors at different molar ratios. Pure and Al-doped hematite electrodes have been used in a complete *n*-type DSSCs. The kinetics of charge transfer through the interface dye/electrolyte was studied and compared to that of a typical *p*-type DSSC based on NiO photocathodes sensitized with erythrosine B. The results suggest a potential application of both Fe_2O_3 and $Fe_2O_3/AlFe_2O_4$ as photoanodes of a *tandem* DSSC.

Keywords Hematite · Al-doped · Dye solar cell · Hercynite · Tandem solar cell · Energy conversion

M. Congiu (✉) · O. Nunes-Neto · C. F. Graeff
UNESP–Univ. Estadual Paulista, POSMAT-Programa de Pós-Graduação em Ciência e Tecnologia de Materiais, Av. Eng. Luiz Edmundo Carrijo Coube 14-01, Bauru, SP 17033-360, Brazil
e-mail: mirko.congiu@fc.unesp.br

M. L. De Marco · M. Bonomo · D. Dini
DC-FC-UNESP–Univ. Estadual Paulista, Av. Eng. Luiz Edmundo Carrijo Coube 14-01, Bauru, SP 17033-360, Brazil

C. F. Graeff
Department of Chemistry, University of Rome "La Sapienza", Piazzale Aldo Moro 5, Rome, RM, Italy

Introduction

Dye-sensitized solar cells (DSSCs) (O'regan and Gräzel 1991) are photoelectrochemical cells which represent an advanced technology of solar conversion with low costs of fabrication and efficiencies up to 13% (Mathew et al. 2014). A typical DSSC configuration consists of a mesoporous semiconductor deposited on a transparent conductive oxide layer (TCO). An organic or organometallic dye is anchored on the surface of the semiconductor and is responsible for light harvesting through the promotion of electrons from the HOMO to the LUMO level of the dye sensitizer. Such an excitation generates charge carriers (electron and hole) at the dye-semiconductor interface thus generating a photopotential. In a *n*-type DSSC, the promoted electron of the excited dye is injected into the conduction band of

Springer

the mesoporous semiconductor (TiO₂ or ZnO). Successively, a redox mediator transfers an electron to regenerate the oxidized dye and is converted into its oxidized form. Contrariwise, in a *p*-type solar cell, the excited electrons of the dye are transferred directly to the redox mediator while the hole is injected in the valence band of the photocathode, namely NiO (Awais et al. 2011; Bonomo; Dini 2016a; Congiu et al. 2016a). In both *p*- and *n*-type DSSCs, the redox mediator is regenerated at the counter-electrode (CE) which consists of a thin layer of catalytic material. Usually, a thin layer of platinum nanoparticles is used as CE for DSSCs (Fu et al. 2012; Lan et al. 2010). However, Pt is an expensive and scarcely available material and its employment in DSSCs influences heavily the overall costs of such devices. Cheaper and more abundant materials, such as CoS, could be used to replace Pt CEs in DSSCs (Congiu et al. 2015a, 2015b, 2016b). However in most applications, CE is not a photoelectroactive element and it serves just as a catalyst for the electrolyte regeneration (De Rossi et al. 2013; Wang and Hu 2012; Wang et al. 2009). A modern strategy to enhance the performance of a DSSC is the adoption of the *tandem* cell configuration, first proposed by He et al., which consists in the replacement of the CE with a dye-sensitized *p*-type electrode (He et al. 2000). In this configuration, the *n*-type photoanode is coupled with a *p*-type photocathode in order to improve the cells performance and enhance the photovoltage (De Vos 1980). However, the efficiency of the *p*-type side is still too low in comparison with the *n*-side, and this leads to a non-cumulative efficiency in *tandem* configuration (Awais et al. 2011; Bonomo and Dini 2016b). Therefore, the use of a sensitized NiO photocathode in *tandem* with a sensitized TiO₂ photoanode, after all, results in a reduction of the performance of the DSSC with the sole photoactive anode. This is mainly due to the lower photocurrent generated by the NiO chatode, which limits the value of the maximum current of the device. In the *tandem* configuration, the photoanode and the photocatode are in series, and the maximum current obtainable is the value of current produced by the less efficient electrode. In this research context, the study of photoelectroactive anodes based on cheap and earth-abundant semiconductors is of great interest and is beneficial to the optimization of DSSCs of the *tandem* type. As photoactive anode hematite represents an ideal candidate since it is a cheap and widely available and displays interesting electrical and optical properties, in fact, hematite possesses

semiconducting properties with an optical band gap of 2.1 eV and *n*-type behavior in most applications (Kumar et al. 2012; Tamirat et al. 2016). The concentration and the nature of charge carriers (electrons) are determined by the existence of oxide vacancies into the lattice (Miller et al. 2004). In particular conditions, it is possible to obtain also hematite of *p*-type as reported by Lin et al., who succeeded in the synthesis of *p*-type hematite via atomic layer deposition and Mg-doping (Lin et al. 2012). In this work, we investigated the electrochemical properties of porous layers of hematite (α-Fe₂O₃), obtained by thermal decomposition of a chemical precursor based on an acetylacetonate (Willis et al. 2007). Through the use of a printing system and a large area deposition method, we could obtain nanostructured layers of α-Fe₂O₃ nanoparticles. In order to study a possible strategy for the improvement of the photoelectrochemical performance of hematite, the doping of iron oxide with different concentrations of aluminum (Al) was considered. Aluminum doping can increase the optical band gap of hematite (Lin et al. 2011). Furthermore, there are several evidences on the improvement of the hematite performance as anode of photoelectrochemical cells induced by Al-doping (Lin et al. 2011; Shinde et al. 2011). The generation of an anodic current in photoelectrochemical cells for water-splitting confirms the *n*-type nature of both pure and Al-doped hematite (Kumar et al. 2012; Shinde et al. 2011). The electrodes were sensitized with two different dyes: one based on Ru (N3) and the organic D5. Complete *n*-type DSSC cells have been fabricated and characterized using sensitized hematite photoanodes. By means of electrochemical impedance spectroscopy (EIS), the charge transfer kinetics at the interface photoanode/ electrolyte has been studied. The results showed a recombination kinetics very close to that observed in a typical *p*-DSSC based on a mesoporous NiO photocathode which is sensitized by erythrosine B.

Materials and methods

Iron (III) chloride, potassium iodide (KI), iodine (I₂), absolute ethanol (EtOH), α-terpineol, ethyl cellulose (EC), acetylacetone (acac), erythrosine B (ERY), cis-Bis(isothiocyanato)bis(2,2′-bipyridyl-4,4′-dicarboxylato ruthenium (II) (N3), and fluorine doped tin oxide coated glass slides (FTO ~ 7Ω/□) were purchased from Sigma-Aldrich and were used as received.

D5 dye (3-(5-(4-(diphenylamino) styryl) thiophen-2-yl)-2-cyanoacrylic acid) was supplied by Dyenamo, Sweden. X-Ray diffraction patterns (XRD) were collected on powder samples with a DMAX Ultima (Rigaku International Corporation, Tokyo, Japan), operating at 40 kV and 2 mA. Scans were performed from 5° to 80° with a step size of 0.02° at the scan speed of 2°/min. Confocal optical microscopy measurements were performed using a Leica DCM 3D Dual Core 3D Measuring Microscope. Imaging with 3D topography allowed the graphical evaluation of the mean square roughness of the surface (RMS) of the hematite electrodes. The surface of the electrodes was also characterized using an atomic force microscopy (AFM) of the type Park Systems XE7. The measurements were performed in the contact mode through the scanning of X,Y-directions to avoid artifacts. The AFM tip was from PPP-CONSTCR Nanosensors and had a force constant of 0.2 N/m and radius < 10 nm. The AFM tip worked at the resonance frequency of 23 kHz. EIS spectra were collected on symmetric devices at 0 V with a sinusoidal modulation of 10 mV from 100 mHz to 100 kHz. The EIS characterization was performed with an Autolab PGStat 300, which was equipped with a FRA32 impedance board. Cyclic voltammetry (CV) was carried out utilizing the same equipment of EIS determinations. Voltammograms were recorded varying the applied potential from −1.0 to 1.0 V at different scan rates. Current vs voltage curves (JV) have been performed in order to calculate the principal photovoltaic (PV) parameters: fill factor (FF), short circuit current (J_{sc}), open circuit voltage (V_{oc}), and efficiency ( ). For further information about PV parameter calculation, please see electronic supplementary material (S.1.).

Preparation of α-Fe$_2$O$_3$ nanoparticle paste

Iron (III) acetylacetonate (Fe (acac)$_3$) has been synthesized with the following procedure: 0.33 g of finely ground FeCl$_3$·6H$_2$O were dissolved in 2.5 mL of distilled water. A fresh-prepared solution of 0.38 g of acetylacetone in 10 mL of methanol was slowly dropped into the main solution under stirring. A solution of 0.51 g of sodium acetate was slowly dropped under stirring into the resulting solution. The mixture was then heated to 80 °C on a hotplate for 15 min and cooled down to room temperature through its immersion in an ice bath. Red crystals were obtained and were separated by suction filtration. The product was washed with cold

water and ethanol and finally dried under vacuum. Al (acac)$_3$ was prepared following the same procedure described above, using Al$_2$ (SO$_4$)$_3$ instead of FeCl$_3$. Al-doped nanoparticles were obtained by mixing Al (acac)$_3$ with Fe (acac)$_3$ in different percentages (0, 1, 5, and 10% w/w) prior to thermal degradation. In order to mix efficiently the precursors, the exact quantities were dissolved in a minimum aliquot of acetone; then, the solvent was slowly evaporated and the resulting powder was finally grinded in a mortar. Spherical α-Fe$_2$O$_3$ and Al$_x$Fe$_{2-x}$O$_3$ nanoparticles (NPs) have been obtained by firing the mixtures of the chemical precursors in a ceramic crucible at 450 °C for 30 min. A ceramic plate was placed under the crucible to avoid any spills into the oven. The obtained products were finely grinded using an agate mortar. In a plastic container, 30 mg of grinded α-Fe$_2$O$_3$ or Al$_x$Fe$_{2-x}$O$_3$ NPs were dispersed in 300 µL of absolute ethanol, and then, 30 mg of EC were added to the slurry. The vessel was transferred in an ultrasound bath and kept in it for 30 min. After the addition of 200 µL of deionized water, the sonication step was repeated. Finally, 20 µL of a 50/50 mixture of acetyl acetone and α-terpineol was added to the slurry. After the addition, the paste was sonicated for more than 30 min. If aggregates are formed, a glass rod should be used to mix the paste.

Deposition of hematite electrodes

FTO (2 × 2cm) square glass slides were thoroughly cleaned using an ultrasonic bath with three different solvents: distilled water, acetone, and isopropanol. Finally, the substrates were dried and used without other treatments. A conventional adhesive tape was used to delimitate a rectangular deposition area of 0.25 cm^2. The paste was then spread on each substrate using a glass slide (doctor blade). The deposited films were dried for 20 min till the complete evaporation of ethanol. After removing the tape mask, the electrodes were transferred into a muffle and annealed at 450 °C for 30 min in order to eliminate all organic components and effectuate the sintering of the metal oxide nanoparticles.

Photoanode sensitization

After the thermal treatment, the oxide films were cooled to 80 °C and rapidly immersed in a solution of D5 in ethanol for 16 h. The sensitizing solution of D5 had a mass concentration of 1 mg/mL. The sensitized

photoanodes were washed several times with absolute ethanol and dried under vacuum. Finally, the electrodes were sealed with a Pt CE using a hot-melt spacer (35 μ, Bynel®). The iodine-based liquid electrolyte HSE-BV12 (Dyers, Roma) was injected by vacuum back-filling. The sealed cells were let to stabilize for 1 h in dark conditions. The determination of the JV curves was realized on the closed DSSCs.

Photometric determination of Fe^{3+} and Al^{3+}

The oxide samples were obtained as powders from the procedures described in previous paragraphs. Ten milligrams of oxide was dissolved into 40 mL of concentrated HCl (37%) with the addition of 1 mL of hydrogen peroxide (20%). The solution was diluted to a final volume of 100 mL with Milli-Q water. The concentrations of both Fe and Al were determined using the photometer Alkafit Superfoto (SN. E008145).

Thiocyanate (SCN^-) was used as colorimetric indicator at fixed wavelengths for the determination of Fe^{3+} (480 nm, blue filter), while eriochrome cyanine was the indicator of Al^{3+} (535 nm, green filter) (Dougan and Wilson 1974; Shull and Guthan 1967). Molar concentrations of Fe and Al were calculated using calibration curves.

Results and discussion

The powder obtained by thermal degradation of pure Fe (acac)$_3$ was characterized through X-ray diffraction (XRD) spectroscopy in order to determinate the phase and the average size of the Fe_2O_3 crystals. As shown in Fig. 1, the powder presents just the hematite phase without other phases of Fe (III) oxide. The pattern shown by the powder is typical of hematite α-Fe_2O_3 (JCPDS 86-0550). Narrow peaks indicate the presence of most nanosized material. When Al (acac)$_3$ was added into precursor mixture, the XRD patterns of the powders obtained by thermal degradation indicated the existence of a second crystal phase. Three new peaks at 30.4°, 43.5°, and 63.1° were assigned, respectively, to (220), (400), and (440) planes of AlFe$_2$O$_4$ (hercynite JCPDS 007-0068) (Fukushima et al. 2013; Jastrzębska et al. 2015). The peak at 57.5 can be assigned to both α-Fe_2O_3 and AlFe$_2$O$_4$. It corresponds to planes (122) and (422), respectively. Such a peak becomes more intense and broader upon addition of increasing amounts of Al.

The XRD peaks associated to AlFe$_2$O$_4$ are broader in comparison with those of α-Fe_2O_3. This suggests that the average crystal size of AlFe$_2$O$_4$ is lower than that of α-Fe_2O_3. Sherrer equation has been used to calculate the average crystal size of both hercynite and hematite. Full widths at half maximum (FWHM) of the peaks were calculated by fitting each of them with a Gaussian function. The resulted average crystal sizes calculated for α-Fe_2O_3 were 32.6 nm for pure hematite and 27.4, 27.7, and 28.6 nm for the powders obtained by firing the mixtures containing 1, 5, and 10% (w/w) of Al (acac)$_3$, respectively. From the peaks at 30.4° and 43.5° (Fig. 1b, c, d), we calculated the average size of AlFe$_2$O$_4$ crystals: 10.8 nm. The latter signals are assigned to hercynite phase.

As a result, the presence AlFe$_2$O$_4$ leads to a reduction of the average crystal size of α-Fe_2O_3 into the mixed oxide phase. From the hematite peaks of the planes (104) and (110) at 33.2 and 35.6°, respectively (Fig. 1a), one can notice an Al-dependent variation of their relative intensities. In fact, in pure hematite, the peak at 33.2° is the more intense signal of the pattern. The addition of Al leads to a systematic reduction of peak intensity at 33.2° and to the increase of that at 35.6°. Looking at the pattern of Fig. 1d, the peak at 35.6 becomes the more intense signal. This suggests that Al influences the preferred orientation of α-Fe_2O_3 crystals when Al(acac)$_3$ weight ratio is higher than 5% (w/w).

Quantification of aluminum

The percentage in weight ratio (w/w) of aluminum in oxide samples was obtained by photometric measurements. The chemical analysis results are resumed in Table 1 and compared with the predicted (theoretical) compositions. The latter are calculated through the mass ratios of chemical precursors in the mixture. Notice that aluminum and iron acetylacetonates have different molecular weights: 324.31 and 353.17 g mol^{-1}, respectively.

As shown in Table 1, mixtures B, C, and D led to the production of oxides with different Al-content. The Al/Fe mass ratio, determined through photometry measurements, showed values close to those calculated considering the composition of mixtures A, B, C, and D. Since XRD patterns have shown the presence of AlFe$_2$O$_4$ (hercynite), it is important to consider that in this phase, iron is present as both Fe^{2+} and Fe^{3+} (Fukushima et al. Takizawa 2013; Jastrzębska et al. 2015). Thus, the

Fig. 1 X-ray diffraction pattern of the powders obtained by firing the mixtures of the chemical precursors at 400 °C during 30 min. **a** The XRD diffraction pattern obtained when no $Al(acac)_3$ was present displays the characteristic peaks of hematite (*white diamond*) (JCPDS 86-0550). The Miller indexes of the diffraction planes (h k l) for pure hematite are on going from left to right in the spectrum: (012), (104), (110), (113), (024), (116), (122), (214), and (300). Diffraction peaks (*black star*) of $AlFe_2O_4$ (hercynite JCPDS 007-0068) begin to appear in the

patterns when $Al(acac)_3$ was mixed with $Fe(acac)_3$ at different percentages (*w/w* %): 1% (**a**), 5% (**b**), and 10% (**c**)
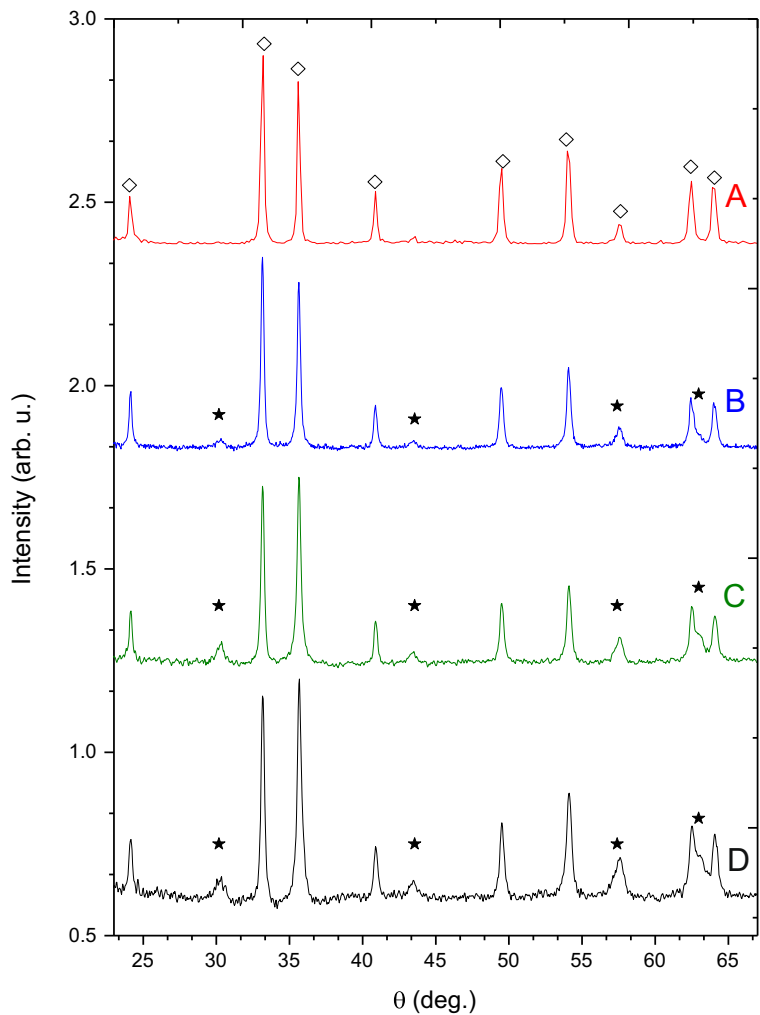
Table 1 Summary of precursor mixture compositions

Precursor mixture	Composition $Al(acac)_3$: $Fe(acac)_3$ (*w/w*) %[a]	Theoretical composition Al/Fe (*w/w* %)[b]	Experimental composition Al/Fe (*w/w* ± α %)[c]
A	0	0	n.d.
B	1	0.53	0.65 ± 0.5
C	5	2.76	2.78 ± 0.3
D	10	5.84	5.61 ± 0.6

[a] Precursor mixtures were obtained by mixing $Al(acac)_3$ and $Fe(acac)_3$ in different mass ratios (0, 1, 5, and 10%)

[b] The theoretical Al/Fe mass ratio was calculated considering $Al(acac)_3/Fe(acac)_3$ mass ratio

[c] Spectrophotometry was employed to determine the Al/Fe mass ratio into the final product (oxide)

n.d. not detected

addition of concentrated H_2O_2 became compulsory in order to precisely quantify the real amount of iron in the samples, as the photometric method is specific solely for Fe^{3+}. As a matter of fact, a good match between the theoretical and the real Al-content in the oxide should depend just on the purity of the starting reagents provided that external contamination sources are minimized.

Porous hematite layers showed a rough surface (Fig. 2a) without any crack or hole. The roughness (RMS) was calculated by confocal microscopy and was in the range 960–850 nm. The film thickness was also determined through confocal topographical analysis (Fig. 2b). The average thickness of porous layers was 4.2 ± 0.5 μm ($n = 3$). Such morphology was obtained after firing the paste since all organic components are burned out leaving empty spaces between sintered nanoparticles. From microscopy images, we also can notice a
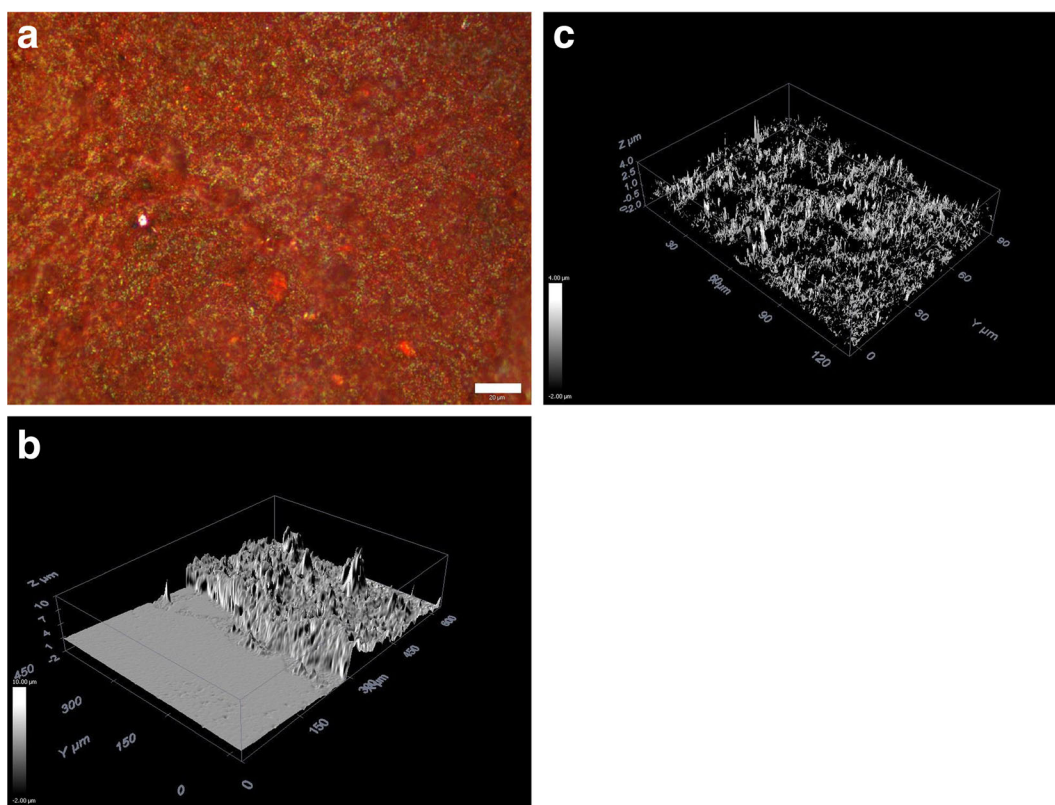
Fig. 2 Confocal microscopy images of the surface of Fe_2O_3 photoanodes: a true color micrograph of the surface with 20× magnification (**a**), the size of the *white bar* was 2 μm; 3D topography of a border region of the electrode (**b**), the FTO substrate appears as a flat region; 3D topography of a central region of the porous film using 100× magnification (**c**), the pores appear as black holes on the surface

macroporous[1] structure of surface. Notice that a porous surface is preferred in DSSC due to the higher surface area, higher dye loading, and the easier penetration and diffusion of the electrolyte (during the operation of the device). In addition to that, the presence of macropores offers the possibility to explore other redox mediators with larger structure such as cobalt (II/III) bipyridine shuttles. In fact, redox mediators consisting of big organometallic complexes possess low diffusion coefficient and large pores generally facilitate their diffusion through the cells (Heo et al. 2012; Trang pham et al. 2014). As shown in Fig. 2c, a higher magnification of the surface, presents pores with a size in the range 10–30 μm.

Atomic force microscopy has been performed on solid film samples in order to obtain morphological information such as nanoparticle shape and size. Figure 3 represents two different nanoparticle films, obtained by firing different precursor mixtures.

As shown in Fig. 3a, the step of thermal degradation of pure Fe (acac)$_3$ (mixture A) leads to the formation of round hematite nanoparticles with an average radius of 54 ± 16 nm (the average is determined from 100 samples). Equation 1 describes the degradation (combustion) reaction between the precursor and oxygen.

$$4\,Fe(C_5H_7O_2)_{3\,(s)} + 72\,O_{2\,(g)} \rightarrow 2\,Fe_2O_{3(s)}$$

$$+\,42\,H_2O_{(g)} + 60\,CO_{2\,(g)} \qquad (1)$$
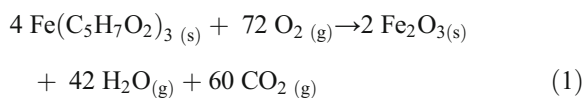
As confirmed by XRD (Fig. 1a), the oxide obtained by firing mixture A has shown just the hematite (α-Fe_2O_3) crystal phase. Thermal treatment of the paste containing Al leads to the formation of Al-doped nanoparticles. As shown in Fig. 3b, the morphology of the film obtained using mixture D presented smaller nanoparticles (25 ± 5 nm). Al-containing nanoparticles appear to be more compact and form relatively large blocks with some cracks.

---

[1] Pores had a linear size larger than 50 nm.

Fig. 3 AFM image of the surface of a thin layer of Fe_2O_3 nanoparticles, obtained by thermal degradation of pure $Fe(acac)_3$ on FTO (**a**). The image **b** represents the morphology of the films obtained using mixture D
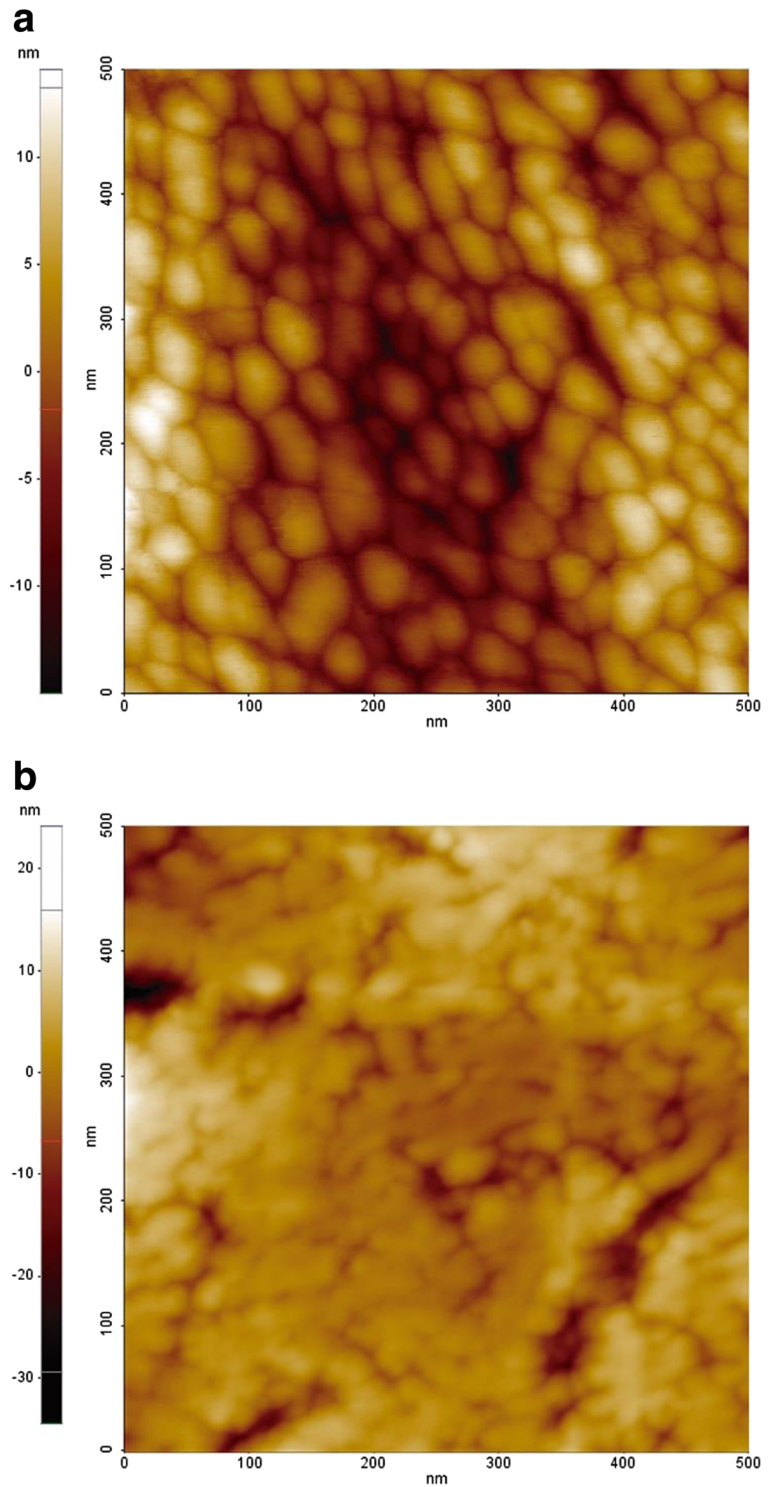
Sensitized electrodes were characterized as photoanodes of DSSCs under simulated sun light (AM 1.5, 1 sun) using platinized FTO as CE. In Fig. 4, the current/voltage responses of three different hematite-

based DSSCs are represented. The first cell setup (A) consists of a porous layer of hematite, obtained with the method described in the previous section. In order to determine the photovoltaic efficiency of the sole hematite, in one configuration, no sensitization was considered. The second and third configurations consist of, respectively, a porous hematite film sensitized with N3 (B) and D5 (C): in these configurations, electrodes were dipped into the dye solution for 8 h.

Under simulated sun light, all photoanodes have produced expectedly anodic photocurrents. In absence of sensitization, pure hematite produced low photocurrent and a photovoltage. As expected, the efficiency of the cell with no dye was the lowest of the sample set. The absorption of organometallic dye N3 on the hematite anodes surface leads to a significant increase of the PV performance. However, better performance has been obtained with D5 dye which has shown the largest PV parameters within this set of samples. In order to improve the cell efficiency, the dyeing time was extended to 16 h, and the measurements were performed in the same experimental conditions (Fig. 4). All results are summarized in Table 2. By prolonging the dipping time, we noticed a significant increase in the photocurrent densities of both D5- and N3-sensitized hematite photoanodes. The gain in photocurrent density was about 20% of the values obtained from the films dipped for 8 h in the dyeing solution. This is probably due to a similar diffusion coefficient of the dyes inside the porous Fe_2O_3 layer. A longer dyeing time increases the

quantity of absorbed dye in the active sites of the mesoporous oxide. Thus, a higher quantity of electrons is injected into the conduction band of hematite generating a higher photocurrent. As shown in Table 2, for D5, we noticed an improvement of the FF and the efficiency of the cell sensitized for 16 h. Probably, the higher quantity of absorbed dye influences the overall electron injection efficiency at the photoanode surface. This is also confirmed by a significant improvement of the cell efficiency (about 30% higher). Also, with N3 dye sensitizer, we have observed an enhancement of the PV characteristics of DSSCs upon prolongation of the dyeing time. In fact, the cell efficiency showed an increase of about 20%.

The measurements were performed under simulated sunlight AM 1.5 (1 sun)

Doping with different percentages of Al

The isovalent substitution of Fe^{3+} with Al^{3+} was considered in order to increase both band gap and charge carrier concentration of the semiconductor. The replacement of Fe^{3+} with Al^{3+} ions in the mixed oxide was performed by using different mixtures of acetylacetonate complexes of the two metals. The changes in optical absorption were registered on samples made of thin layers of nanoparticles deposited onto FTO with percentages of $Al(acac)_3$ varying from 0 to 10%. The UV-Vis absorption spectra of the various samples are represented in Fig. 5.

Fig. 4 Current vs voltage response of hematite-based dye solar cells. A pure layer of porous hematite (*black triangle*) with no absorbed dye was used for comparison. Porous hematite layers were sensitized with N3 for 8 (*black star*) and 16 h (*white star*). Also, the dyeing with the organic D5 was considered for 8 (*white square*) and 16 h (*white circle*). The measurements were performed on sealed cells using HSE bv12 iodine-based electrolyte under the light of a sun simulator (AM 1.5; 1 sun)
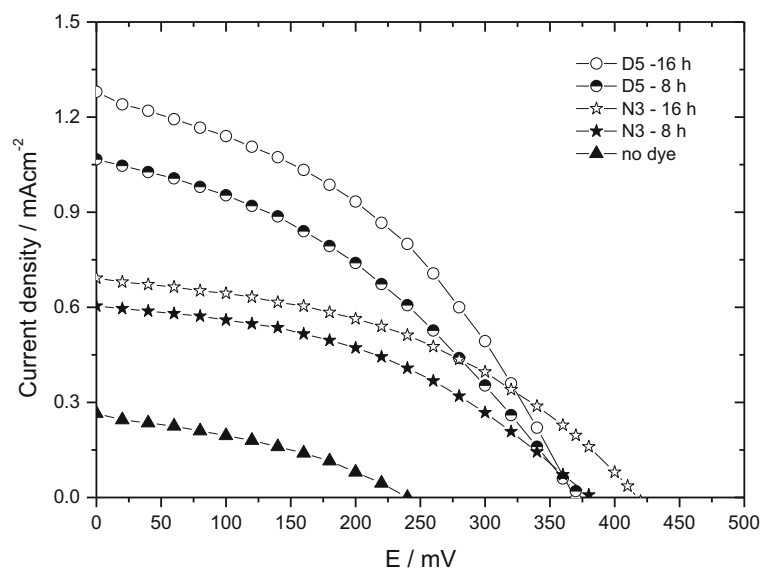
Table 2 Summary of the PV parameters of different solar cells based on two different photoelectrodes: hematite photoanodes (*n*-type) and, for comparison, NiO (*p*-type) sensitized with erythrosine (EryB) and P1

Material	DSSC type (n/p)	Dye	Dipping time (h)	Jsc (mAcm^{-2})	Voc (V)	FF (%)	Eff (%)	Reference
TiO$_2$	n	D5	16	11.040	0.619	58.0	3.99	(DESSI et al., 2014)
TiO$_2$	n	N3	16	19.220	0.720	67.4	9.33	(ADACHI et al., 2004)
Hematite	n	D5	16	1.280	0.370	41.8	0.198	this work
Hematite	n	N3	16	0.692	0.418	42.2	0.122	this work
Hematite	n	D5	8	1.060	0.370	37.4	0.147	this work
Hematite	n	N3	8	0.604	0.380	42.7	0.098	this work
Hematite	n	–	–	0.265	0.240	35.0	0.022	this work
Hematite	n	Ruthenizer 535-bisTBA	12	0.250	0.420	38.0	0.04	(Rashid; Kishi; Soga, 2016)
NiO	p	EryB	24	−0.412	−0.125	35.8	0.022	(Novelli et al., 2015)
NiO	p	SQ2	7	−0.693	−0.132	37.6	0.041	(Novelli et al., 2015)
NiO	p	P1	16	−2.84	−0.125	33.7	0.121	(Gibson et al., 2013)

The determination of the direct band gap (E_g) of the films was accomplished through Tauc plots utilizing the UV-Vis spectra of the films. Pure α-Fe$_2$O$_3$ thin films exhibited an E_g of 2.1 eV, a value characteristic of hematite (Shinde et al. 2011; Tamirat et al. 2016). Films obtained by firing mixture B (1% Al(acac)$_3$) had shown a slight decrease of E_g (2.05 eV). Also, mixture C, which contains 5% of Al(acac)$_3$, led to the formation of films with a lower E_g (1.86 eV). Mixture D (10% of Al(acac)$_3$) gave a film presenting a sharp increase of E_g (2.45 eV). Such an effect is also accompanied by the blue shift of the main absorption band in the respective UV-Vis spectrum (Fig. 5). For further information about E_g data and measurements, please refer to S.I. In Fig. 6, one can see that mixture D formed films with a lower absorbance in the region 340–600 nm. Contrariwise, films obtained using mixture C presented a broad peak in the region 575–700 nm.

With the same method reported in the experimental section, Al-doped nanoparticles have been obtained and used to prepare dense and spreadable pastes. Al-doped hematite photoanodes have been deposited and sintered

Fig. 5 Absorbance spectra of thin layers of Al-doped Fe$_2$O$_3$ on FTO. Different concentration ratios (*w/w*) of Al(acac)$_3$ were used in precursor mixtures A, B, C, and D: 0 (*black triangle*), 1 (*black star*), 5 (*white circle*), and 10% (*white star*). In order to obtain a quasi-transparent film, only 10 mg of the precursor mixtures were dissolved in 1 mL water/ethanol (50/50 *v/v*) and were deposited on clean FTO at the dosage 100 μL cm^{-2}, and then fired
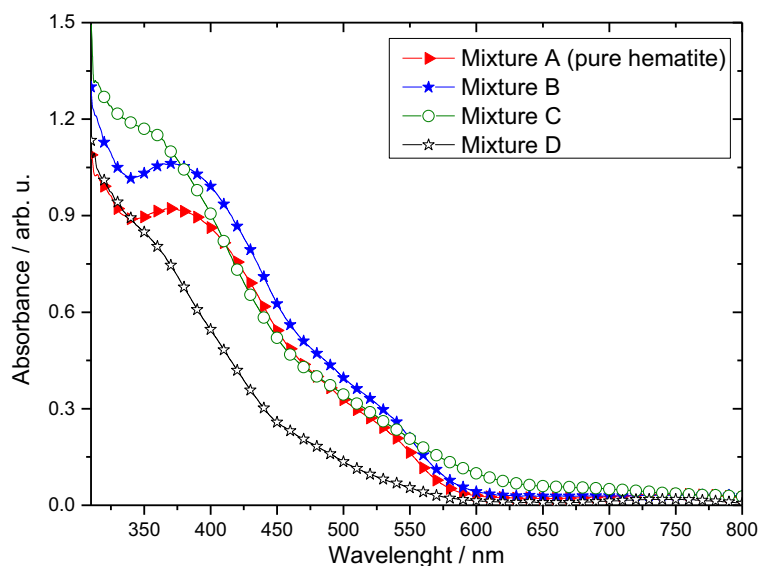
Fig. 6 JV curves of D5-sensitized photoanodes fabricated using different percentages of Al(acac)$_3$ in the precursor mixtures: mixture A: 0% (*black triangle*); mixture B: 1% (*white square*); mixture C: 5% (*white circle*); mixture D: 10% (*black square*). JV measurements were performed under simulated sun light AM 1.5 (1 sun)
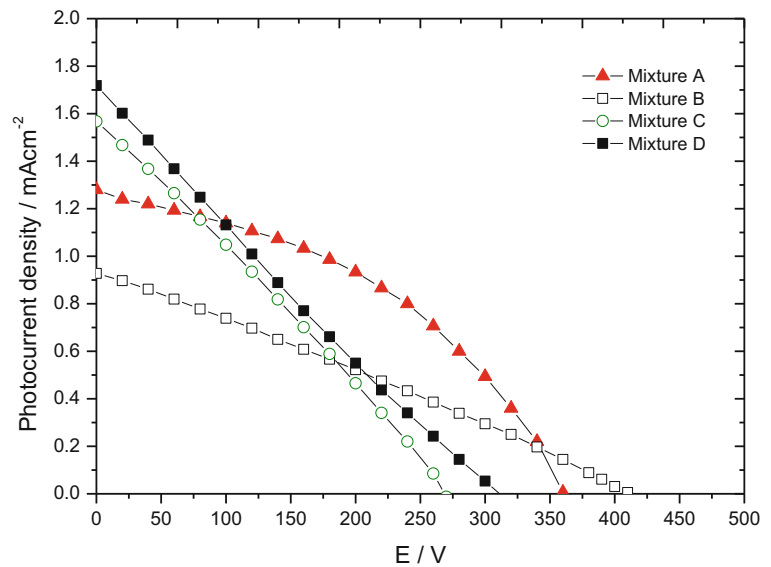
following the same procedure used for pure hematite. The obtained photoanodes have been characterized using only D5 as sensitizer, due to its higher performance with hematite (Fig. 4, vide supra). The PV parameters of the sensitized photoanodes are listed in Table 3, which reports also the compositions of the respective precursor mixtures.

From Table 3, it resulted in the increase of J_{sc} as a function of Al-content in the precursor mixture (Tables 1 and 3, second column). This effect can be explained considering the effect of Al-doping, on hematite's electronic properties. In fact, it was reported by Kleiman-Shwarsctein et al. in 2010 that the charge carrier density was in the range of $4–7 \times 10^{21}$ cm^{-3} for pure electrodeposited hematite and 1.3×10^{22} cm^{-3} for the Al-doped sample (Kleiman-Shwarsctein et al. 2010). In their experiments, Kleiman-Shwarsctein used a percentage of Al of 10%. This effect on the charge carrier density was also reported by Shinde et al. in 2011, in sputtered Al-doped hematite films (SHINDE et al. 2011). In the experiment described in this work, the increase of the Al/Fe mass ratio (from 0 to 5.61%) leads to sensible reduction of V_{oc} and of FF. As a result, lower efficiencies were obtained when mixtures B, C, and D were used to prepare Al-doped nanoparticles (Fig. 6 and Table 3). As confirmed from EIS spectra (Fig. 7), Al-doped hematite showed a lower charge transfer resistance. This renders the recombination of the injected electron with the electrolyte more favorable instead of its diffusion to the external contact. The higher recombination rate of electrons at the electrolyte/

photoanode interface influences negatively the fill factor of the cell. In fact, as shown by JV plots (Fig. 6), the higher the Al content the higher the slope of the curve and the lower the FF. Using photoanodes prepared with the mixture D, the corresponding cell gave $J_{sc} = 1.720$ mAcm^{-2}, i.e., 25% higher than that obtained using pure hematite (mixture A, Table 3). Photoanodes prepared with the mixture C gave cells that produced an increase of about 18% in efficiency with respect to undoped photoanodes. With mixture B, the corresponding photoanode produced a cell with the highest value of open circuit photovoltage within this set of n-DSSCs ($V_{oc} = 410$ mV). Mixture A (pure hematite) showed a good value of J_{sc}. Moreover, the shape of the curve was characterized by a higher FF (41.8%) and a higher efficiency (0.198%). Despite the lower performance obtained with mixture D, there was a significant gain in the device transparency. In fact, from the transmittance values of the photoanodes, one can notice that the semi-transparency of the electrode is obtained using just 10% Al(acac)$_3$ in the precursor mixture (Table 4). The lower absorbance of the photoanode, in a tandem DSSC illuminated from both sides, results in a higher quantity of solar radiation reaching the photocathode.

As a result of the JV characterization, the doping with Al led to a poorer PV performance in all values of concentrations here considered. In order to understand the effect of AlFe$_2$O$_4$ on the photoanode's electrochemistry, EIS measurements (Fig. 7) have been performed on the devices. The spectra were registered in forward

Table 3 PV parameters of different solar cells based on hematite photoanodes prepared using different weight percentages (w/w) of Al $(acac)_3$ in the precursor mixture

Mixture[a]	Al$(acac)_3$	Al:Fe (w:w %)	Dye	J_{sc} (mAcm^{-2})	V_{oc} (V)	FF (%)	η (%)	T_{500}[b] (%)
D	10%	5.61 ± 0.6	D5	1.720	0.310	23.6	0.126	70
C	5%	2.78 ± 0.3	D5	1.560	0.260	28.0	0.113	3
B	1%	0.65 ± 0.5	D5	0.613	0.410	27.9	0.105	0
A	0	nd	D5	1280	0.370	41.8	0.198	0

bias (n-type), applying V_{oc} (negative voltages) as external bias. Notice that, in the EIS setup, the photoanode is the working electrode and Pt is both the counter and the reference electrode. So, all of the applied voltages are considered vs Pt. The negative voltages are required for the forward bias configuration, because hematite is an n-type semiconductor. For further information about the n-type behavior of Al-doped hematite photoanodes, please see S.I. (Mott-Schottky plots). EIS spectra have been fitted in order to extract the key parameters involved in the charge-transfer process. Notice that the charge transfer at the interface dye/electrolyte is an adverse reaction in the whole functioning of the device. In fact, the charge transferred back to the electrolyte does not contribute to the photocurrent nor to the photovoltage. The sole charges which generate the current in the external circuit are those which are conducted from the surface of the semiconductor to the FTO. In a typical DSSC, one can distinguish two separate sides where recombination takes place: the CE and the photoanode (PA) or

photocathode (PC). In this respect, DSSC can be considered as an electronic circuit (equivalent circuit) in which each element (resistor, capacitor, etc.) is associated to a specific process. The inset in Fig. 7 represents the equivalent circuit used for the analysis of both p-DSSC and n-DSSC (BONOMO et al. 2016). The circuit consists of the following: (i) a series resistance, which takes account to the charge transport through the external circuit (R_s); (ii) the resistance term R_{CE} in parallel with the capacitive term CPE, e.g., the constant phase element, representative of the recombination at the CE/electrolyte interface; (iii) a transmission line element modeling the behavior of the porous oxide films (e.g., NiO and Al-doped hematite) at the interface with the electrolyte, which also considers the internal charge transport through the nanoparticles.

Some key parameters related to the charge transport properties of the oxide films can be directly obtained by fitting: the most important ones are the charge transport resistance (R_t) through the

Fig. 7 Nyquist plot of two complete n-type DSSCs using D5 as photosensitizer, absorbed on porous hematite layers of nanoparticles obtained by mixture A (*black square*) and mixture D (*circle with upper half black*). The analysis was performed in the dark applying the respective V_{oc} as forward bias. The forward bias polarization forces the electrons to recombine with the electrolyte simulating the recombination in operational conditions. The inset shows the equivalent circuit (transmission line) used to fit the experimental data and extract the key parameters fundamental for the comparative analysis
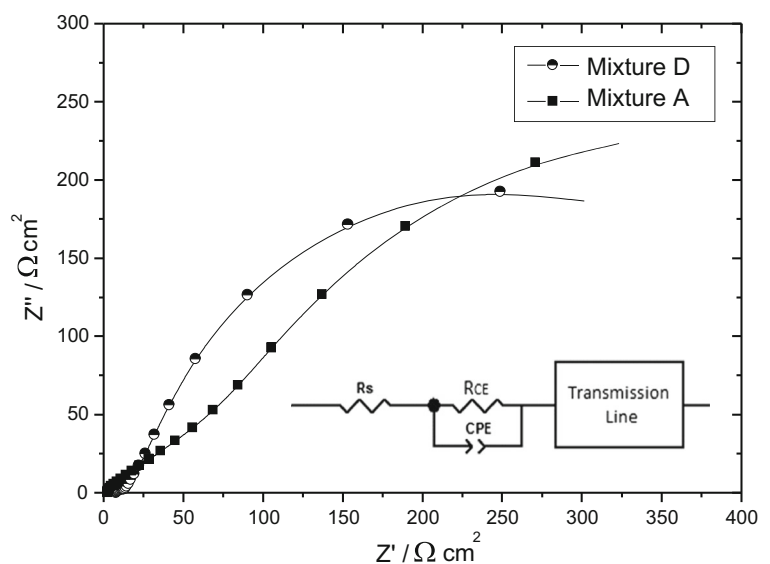
Table 4 Key transport parameter, calculated by fitting the experimental data with the equivalent circuit represented in Fig. 7

Photoelectrode	Type	Dye	$R_t/\Omega\text{cm}^2$	R_{rec} (Ωcm^2)	$C_\mu/\mu\text{F}$
NiO	p	ERY	27.5 ± 0.5	521.8 ± 2.5	439 ± 3
Pure hematite (mixture A)	n	D5	50.4 ± 3.7	817.6 ± 49.5	693 ± 14
Hercynite/hematite (mixture D)	n	D5	13.7 ± 0.4	449.0 ± 5.9	803 ± 11

nanoparticles of the oxide films and the charge transfer resistance (R_{rec}) through PA (or PC) and electrolyte. Furthermore, the chemical capacitance C_μ included in the transmission line (Fig. 7) can be deducted by means of the fitted value of CPE through the relationship $C_\mu = (C_{CPE}{*}R_{rec})^{1/n}/R_{rec}$ where C_{CPE} and n are used as fitting parameters (Fabregat-Santiago et al. 2011; Hirschorn et al. 2010). Other important parameters directly correlated to the terms presented above are (i) the hole (or electron) diffusion time τ_d (=$R_{t*}C_\mu$), which represents the time spent by the photoinjected charge carrier to cross the semiconducting layer, and (ii) the recombination time τ_h (=$R_{rec*}C_\mu$), e.g., the lifetime of the photoinjected charge before it undergoes recombination. As far as the CE of the DSSC is concerned, its characterization and performance evaluation rely on the determination of the term R_{CE}, e.g., the charge transfer resistance at the CE/electrolyte interface, and of the term CPE describing the capacitance of the double layer generated at the same interface.

The values represent the charge transfer kinetic at the interface photoelectrode/electrolyte. In the transmission line model, the term R_t takes in account the internal resistance of the porous oxide films. The charge recombination at the interface with the electrolyte is represented by two values: the recombination resistance (R_{rec}) and the double layer capacitance C_μ

As shown in Table 4, Al doping modifies the charge transport properties of the porous oxide film. In fact, one can see a significant reduction of the term R_t which changes from 50.4 ± 3.7 to 13.7 ± 0.4 Ωcm^2 upon addition of 10% Al(acac)$_3$ to the precursor mixture. This effect can be explained with the increase of conductivity from 3.58×10^{-2} for pure hematite to 3.70×10^{-2} $(\Omega\text{m})^{-1}$ for 10% Al-doped films, as observed also by Shinde et al. (2011). Notice that 10% of Al(acac)$_3$ does not mean 10% of Al in the final product (Table 1). Another effect of the presence of Al into the hematite films is the reduction of the R_{rec} which makes recombination more favorable. For this reason, when

an Al-doped electrode was used as photoanode, the respective JV curves show a higher slope in comparison with those obtained using pure hematite. This effect affects directly the FF of the cell and thus the overall efficiency. However, when Al(acac)$_3$ is mixed at 10% (w/w) with Fe(acac)$_3$, a transparent electrode was obtained (mixture D, Fig. 5). So, this concentration could be considered in order to produce an optically performing photoactive "counter electrode" for a *tandem p*-DSSC. In fact, as shown in Table 3, this photoanode, sensitized with D5, produces photocurrents compliant with that of a typical *p*-DSSC based on NiO sensitized with ERY.

Conclusions

A print-compatible method, based on non-expensive chemical precursors, was here proposed for the deposition of *n*-type nanoparticles of pure hematite and its Al-doped versions on conductive FTO. The proposed method consists of the thermal degradation of a precursor mixture, which allows the easy and non-expensive fabrication of sintered photoanodes. The inclusion of aluminum into the precursor mixture leads to a mixed phase hematite/hercynite with different optical and electrochemical characteristics. The as-deposited layers were dyed with N3 and D5 sensitizers, two dyes commonly employed in DSSCs based on TiO$_2$ mesoporous photoanodes. In working conditions, the photoanodes sensitized with D5 (organic) resulted more efficient than those sensitized with N3 (organometallic). For this reason, D5 was further considered for a more in-depth electrochemical characterization in order to understand the effect of the presence of Al^{3+} on the cell's performance. As a result, pure hematite showed higher PV performance in comparison with Al-doped photoanodes. A significant enhancement in the photocurrent was obtained using the photoanode with 5.61% Al/Fe (w/w). In addition to that, this concentration makes the electrode semi-transparent (T % = 70% at 500 nm). With 0.65%

Al/Fe (*w/w*), the cell showed a gain in photovoltage, although the drop in the fill factor leads to a lower efficiency in comparison to that of pure hematite. One of the most important findings of this work is the evidence of a similar recombination kinetics concerning the charge transfers at NiO/ERY/electrolyte and hematite/D5/electrolyte interfaces. Moreover, the photocurrent value compliance makes this electrode particularly interesting in a tandem cell configuration using ERY-sensitized NiO photocathodes. For example, a sandwich of hematite layers doped with increasing concentrations of Al, deposited on pure hematite, could be exploited for combining all advantages in terms of transparency, photovoltage, and photocurrent. The Al/Fe ratio should be studied in the range 0–1% in order to optimize the photovoltage in a future study on complete *tandem* devices.

Compliance of ethical standards

Conflict of interest   The authors declare that they have no conflict of interest.

References

Adachi M et al (2004) Highly efficient dye-sensitized solar cells with a titania thin-film electrode composed of a network structure of single-crystal-like TiO_2 nanowires made by the "oriented attachment" mechanism. J Am Chem Soc 126(45): 14943–14949

Awais M et al (2011) Application of a novel microwave plasma treatment for the sintering of nickel oxide coatings for use in dye-sensitized solar cells. Surf Coat Technol 205:S245–S249

Bonomo M et al (2016) Beneficial effect of electron-withdrawing groups on the sensitizing action of Squaraines for p-type dye-sensitized solar cells. J Phys Chem C 120(30):16340–16353

Bonomo M, Dini D (2016a) Nanostructured p -type semiconductor electrodes and Photoelectrochemistry of their reduction processes. Energies 9(1):373

Bonomo M, Dini D (2016b) Nanostructured p-type semiconductor electrodes and Photoelectrochemistry of their reduction processes. Energies 9(5):373

Congiu M et al (2015a) Single precursor route to efficient cobalt sulphide counter electrodes for dye sensitized solar cells. Electrochim Acta 151(0):517–524

Congiu M et al (2015b) A novel and large area suitable water-based ink for the deposition of cobalt sulfide films for solar energy conversion with iodine-free electrolytes. Sol Energy 122:87–96

Congiu M et al (2016a) Cobalt sulfide as counter electrode in p-type dye-sensitized solar cells. ChemistrySelect 1(11):2808–2815

Congiu M et al (2016b) Cu2-xS films as counter-electrodes for dye solar cells with ferrocene-based liquid electrolytes. Thin Solid Films 612:22–28

De Rossi F et al (2013) Blending CoS and Pt for amelioration of electrodeposited transparent counterelectrodes and the efficiency of back-illuminated dye solar cells. J Mater Chem A 1(41):12941

De Vos A (1980) Detailed balance limit of the efficiency of tandem solar cells. J Phys D Appl Phys 13(5):839

Dessi A et al (2014) Organic dyes with intense light absorption especially suitable for application in thin-layer dye-sensitized solar cells. Chem Commun 50(90):13952–13955

Dougan WK, Wilson AL (1974) The absorptiometric determination of aluminium in water. A comparison of some chromogenic reagents and the development of an improved method. Analyst 99(1180):413–430

Fabregat-Santiago F et al (2011) Characterization of nanostructured hybrid and organic solar cells by impedance spectroscopy. Phys Chem Chem Phys 13(20):9083

Fu N et al (2012) Electrodeposition of platinum on plastic substrates as counter electrodes for flexible dye-sensitized solar cells. J Phys Chem C 116(4):2850–2857

Fukushima J, Hayashi Y, Takizawa H (2013) Structure and magnetic properties of $FeAl_2O_4$ synthesized by microwave magnetic field irradiation. Journal of Asian Ceramic Societies 1(1):41–45

Gibson E (2013) A et al. Dye sensitised solar cells with nickel oxide photocathodes prepared via scalable microwave sintering Pccp 15(7):2411–2420

He J et al (2000) Dye-sensitized nanostructured tandem cell-first demonstrated cell with a dye-sensitized photocathode. Sol Energy Mater Sol Cells 62(3):265–273

Heo JH et al (2012) Sb 2 S 3 -sensitized photoelectrochemical cells: open circuit voltage enhancement through the introduction of poly-3-hexylthiophene interlayer. J Phys Chem C 116(39):20717–20721

Hirschorn B et al (2010) Determination of effective capacitance and film thickness from constant-phase-element parameters. Electrochim Acta 55(21):6218–6227

Jastrzębska I et al (2015) Crystal structure and Mössbauer study of $FeAl_2O_4$. Nukleonika 60(1):47–49

Kleiman-Shwarsctein A et al (2010) Electrodeposited aluminum-doped ??-Fe_2O_3 photoelectrodes: experiment and theory. Chem Mater 22(2):510–517

Kumar, P. et al. 2012 Photoelectrochemical Hydrogen Generation using Al Doped Nanostructured Hematite Thin Films BT - Chemistry of Phytopotentials: Health, Energy and Environmental Perspectives. In: Khemani, D. L.; Srivastava, M. M.; Srivastava, S. (Eds.). Berlin, Heidelberg: Springer Berlin Heidelberg. p. 197–200.

Lan JL et al (2010) The simple and easy way to manufacture counter electrode for dye-sensitized solar cells. Curr Appl Phys 10(2):S168–S171

Lin Y et al (2011) Hematite-based solar water splitting: challenges and opportunities. Energy & Environmental Science 4(12): 4862

Lin Y et al (2012) Growth of p-type hematite by atomic layer deposition and its utilization for improved solar water splitting. J Am Chem Soc 134(12):5508–5511

Mathew S et al (2014) Dye-sensitized solar cells with 13% efficiency achieved through the molecular engineering of porphyrin sensitizers. Nat Chem 6(3):242–247

Miller EL et al (2004) Low-temperature reactively sputtered iron oxide for thin film devices. Thin Solid Films 466(1–2):307–313

Novelli V et al (2015) Electrochemical characterization of rapid discharge sintering (RDS) NiO cathodes for dye-sensitized solar cells of p-type. Am J Anal Chem 6(2):176–187

O'regan B, Gräzel M (1991) A low-cost, high-efficiency solar cell based on dye-sensitized. Nature 353:737–740

Rashid NM, Kishi N, Soga T (2016) Effects of nanostructures on iron oxide based dye sensitized solar cells fabricated on iron foils. Mater Res Bull 77:126–130

Shinde SS et al (2011) Physical properties of hematite α-Fe2O3 thin films: application to photoelectrochemical solar cells. J Semicond 32(1):13001

Shull KE, Guthan GR (1967) Rapid modified eriochrome cyanine R method for determination of aluminum in water. Journal (American Water Works Association) 59(11):1456–1468

Tamirat AG et al (2016) Using hematite for photoelectrochemical water splitting: a review of current progress and challenges. Nanoscale Horizons 1(4):243–267

Trang Pham, T. T. et al. (2014) Reducing mass-transport limitations in cobalt-electrolyte-based dye-sensitized solar cells by photoanode modification. Chem Phys Chem. Anais

Wang H, Hu YH (2012) Graphene as a counter electrode material for dye-sensitized solar cells. Energy & Environmental Science 5(8):8182

Wang M et al (2009) CoS supersedes Pt as efficient electrocatalyst for triiodide reduction in dye-sensitized solar cells. J Am Chem Soc 131(44):15976–15977

Willis AL et al (2007) Metal acetylacetonates as general precursors for the synthesis of early transition metal oxide nanomaterials. Journal of Nanomaterials, v 2007